

First Principles Predicting Enhanced Ductility of Boride Carbide through Magnesium Microalloying

Bin Tang,¹⁺ Yi He,¹⁺ William A. Goddard III,² and Qi An^{3*}

¹State Key Laboratory of Electronic Thin Films and Integrated Devices, University of Electronic Science and Technology of China, Chengdu 611731, China

²Materials and Process Simulation Center, California Institute of Technology, Pasadena, California 91125, United States

³Department of Chemical and Materials Engineering, University of Nevada-Reno, Reno, Nevada 89557, United States

*Corresponding author-Email: qia@unr.edu

⁺B.T and Y.H. contributed equally to this work.

Abstract: The low fracture toughness of strong covalent solids prevents them from wide engineering applications. Microalloying metal elements into covalent solids may lead to a significant improvement on mechanical properties and drastically changes on the chemical bonding. To illustrate these effects we employed density functional theory (DFT) to examine the bonding characteristic and mechanical failure of recent synthesized magnesium boride carbide ($\text{Mg}_3\text{B}_{50}\text{C}_8$) that is formed by adding Mg into boron carbide (B_4C). We found that $\text{Mg}_3\text{B}_{50}\text{C}_8$ has more metallic bonding character than B_4C , but the atomic structure still satisfies Wade's rules. The metallic bonding significantly affects the failure mechanisms of $\text{Mg}_3\text{B}_{50}\text{C}_8$ compared to B_4C . In $\text{Mg}_3\text{B}_{50}\text{C}_8$, the B_{12} icosahedral clusters are rotated accommodated to the extensive shear strain without deconstruction. In addition, the critical failure strength of $\text{Mg}_3\text{B}_{50}\text{C}_8$ is slightly higher than that of B_4C under indentation stress conditions. Our results suggested that the ductility of $\text{Mg}_3\text{B}_{50}\text{C}_8$ is drastically enhanced compared to B_4C while the hardness is slightly higher than B_4C .

Keywords: $\text{Mg}_3\text{B}_{50}\text{C}_8$, DFT, chemical bonding, mechanical failure

1. Introduction

Boron carbide (B_4C) and related superstrong ceramics, such as boron suboxide (B_6O) and boron subphosphide ($B_{12}P_2$), have been widely used as cutting tools, body armors and in many other industrial applications because of such excellent physical properties as good corrosion resistance, low density, high strength, and high temperature stability.¹⁻¹¹ However, B_4C and related superhard covalent solids are too brittle under high pressure and hypervelocity impact because of the amorphous shear band formation.^{8,9,11,12} Many approaches have been suggested and examined to enhance the ductility of B_4C and related materials by suppressing the amorphous shear band formation.^{10,13-16} Particularly, previous density functional theory (DFT) studies have suggested that doping Si into B_4C can significantly enhance the ductility by suppressing the deconstruction of icosahedral clusters.^{10,16} This was validated by very recent experiment indicating that adding ~1.5at% Si into B_4C exhibits the mitigation of the amorphous shear band formation.¹⁴ Another DFT study showed that making co-crystal of B_4C and B_6O can suppress the failure mechanism of B_4C , improving its ductility.¹³ In addition, the recent study combining transmission electron microscopy experiments and reactive force field (reaxFF) reactive molecular dynamics simulations indicated that decreasing the grain size to nanoscale in B_4C facilitates the grain boundaries (GBs) sliding, enhancing the ductility of polycrystalline B_4C .¹⁵

Recently, adding metals into B_4C has been very attractive because this may drastically change its mechanical, electronic and optical properties. Particularly, the

mechanical properties of B₄C could be enhanced by dopants that can be divided into active doping and inactive doping according to their capability to reacting with B₄C. The active elements mainly include the Si, Ti, Al, etc,¹⁷⁻²² while the inactive elements are Cu, Ag, and Au.²³⁻²⁶ Among active elements, the Si can react with carbon atoms in B₄C at high temperature to form stable silicon carbide (SiC). But the free carbon in B₄C is limited, leading to some of the silicon atoms directly inserting into the crystal lattice of B₄C.^{10,14,20} In addition, Ti can react with B and C atoms to form stable hardening material TiB₂, TiB and TiC.^{27,28} Al can also react with some mounts of B₄C to form Al-BC compounds.²⁹⁻³¹ The main strengthening mechanism of these approaches is that the densification can be promoted through the liquid-phase sintering, the boosted reaction between the additives and B₄C, and the reinforced metal boride phases.

Adding metal elements to B₄C may significantly affect such mechanical properties as elasticity, plasticity, stiffness, hardness, fracture toughness, etc. Therefore, it has been attracted for experimental and theoretical studies on the mechanical properties of metal doped B₄C. Particularly, adding magnesium (Mg) to B₄C results in the formation of Mg₃B₅₀C₈ whose microhardness (Vickers (H_V) of 32.0 GPa)³² is higher than that of B₄C (Vickers of 30.0 GPa)³³. In addition, adding Li to B₄C forming LiB₁₃C₂ (*r*-LiB₁₃C₂) whose crystal structure can be derived directly from the boron very rich boron carbide (B₁₃C₂) as a simple atomic filling.³⁴ However, it remains unknown how the doped metal elements affect the intrinsic deformation and failure mechanisms, which could play an important role in determining the strength

and ductility of these superhard ceramics.

Beside mechanical properties, adding metal elements may significantly affect the chemical bonding and electronic properties of B_4C . Doping metal elements in semiconductors would normally cause metal elements to lose their electrons and become positive ions. B_4C is a high temperature P-type semiconductor material and the doped metal elements may affect the bonding character and the carriers, resulting in the changes of the electronic properties. Therefore, it is essential to explore how the metallic dopants affect the chemical bonding of B_4C .

In this Article, we carried out DFT simulations at the Perdew-Burke-Ernzerhof (PBE) functional level³⁵ to examine the bonding characteristic and shear induced failure mechanism of $Mg_3B_{50}C_8$. We found that the chemical bonding in $Mg_3B_{50}C_8$ still satisfies the Wade's rule in which 26 electrons are required to stabilize the B_{12} icosahedron.³⁶ More interesting, the failure mechanism of $Mg_3B_{50}C_8$ is significantly different compared to B_4C . The icosahedron in $Mg_3B_{50}C_8$ has not been deconstructed under ideal shear deformation up to 0.833 shear strain. While in B_4C , icosahedra are disintegrated at 0.348 shear strain, leading to the amorphous shear band formation.⁹ Under biaxial shear deformation mimicking the indentation stress conditions, icosahedra in $Mg_3B_{50}C_8$ are deconstructed at 0.227 shear strain, which arises from the interaction of C-B-C chain and icosahedral clusters under highly compressive stress conditions.

2. Computational Methodology

The mechanical properties and chemical bonding properties of $Mg_3B_{50}C_8$ were

investigated using periodic DFT approach implemented in VASP package.³⁷⁻³⁹ The Perdew-Burke-Ernzerhof (PBE) functional was employed to describe electronic exchange and correlation interaction. The projector augmented wave (PAW) method was used to generate the pseudopotential that accounts for the core-valence interactions.⁴⁰ The $2p^63s^2$, $2s^22p^1$, and $2s^22p^2$ electrons were treated as valence electrons for Mg, B, and C, respectively. The tetrahedron method with Blöchl correction was applied to account for the electron partial occupancies.⁴¹ For the convergence of DFT simulation, the plane wave cutoff, the energy convergence for self-consistent field (SCF), and force convergence on each atom were set to 500 eV, 10^{-5} eV and 10^{-2} eV/Å, respectively.

The elastic properties of $Mg_3B_{50}C_8$ were investigated by deriving the elastic constant, bulk modulus (B) and shear modulus (G).^{42,43} The elastic constant C_{ij} were computed from the stress-strain relationship which was obtained by distorting the equilibrium lattice configuration along various directions. Then, the stiffness constant S_{ij} was derived through the inverse relation between stiffness constant S_{ij} and elastic constant C_{ij} , which is $S_{ij} = (C_{ij})^{-1}$. Finally, the isotropic polycrystalline elastic moduli (B and G) were computed from stiffness constant and elastic constant by calculating the arithmetic mean of Voigt and Reuss bounds.⁴⁴

To examine the mechanical response and failure mechanism of $Mg_3B_{50}C_8$, we first applied ideal shear deformation by imposing the shear strain on a particular slip system while allowing full structural relaxation along other five strain components. Then we applied biaxial shear deformation to mimic the complex stress conditions in

Vickers indentation experiments. Beneath an indenter, the shear stress (σ_{xz}) and the normal compressive stress (σ_{zz}) satisfy the condition of $\sigma_{zz} = \sigma_{xz} \times \tan \Phi$ where Φ is the centerline-to-face angle of the indenter ($\Phi = 68^\circ$ for Vickers indenter).⁴⁵ To determine the most plausible slip system for $\text{Mg}_3\text{B}_{50}\text{C}_8$, we selected 5 slip systems including (100)[001], (100)[010], (010)[001], (001)[$\bar{1}\bar{1}0$] and (001)[$\bar{1}00$] for the ideal shear deformation. Two slip systems with the lowest ideal shear strength will be considered further for the biaxial shear deformation. The residual stresses after relaxing were less than 0.5 GPa for both ideal shear and biaxial shear deformation. For the shear deformation, we used the supercell containing 61 atoms for (100)[001], (100)[010], and (010)[001] slip systems, and a supercell with 122 atoms for (001)[$\bar{1}00$] and (001)[$\bar{1}\bar{1}0$] slip systems in which the unit cell is replicated twice along [$\bar{1}00$] and [$\bar{1}\bar{1}0$] directions, respectively. The supercell with 122 atoms was employed for (001) slip plane since the (001) plane corresponds to the (01 $\bar{1}\bar{1}$) slip plane in B_4C ,⁹ and it is comparable to our previous simulations on B_4C with 120 atoms in the supercell. We applied the (4×6×4) K-point grid mesh in the Brillouin zone for (100)[001], (100)[010], (010)[001], and (001)[$\bar{1}00$] slip systems, and the (4×4×4) K-point grid mesh for (001)[$\bar{1}\bar{1}0$] slip system in both ideal shear and biaxial shear deformation.

3. Results and Discussion

3.1 Atomic structure and chemical bonding

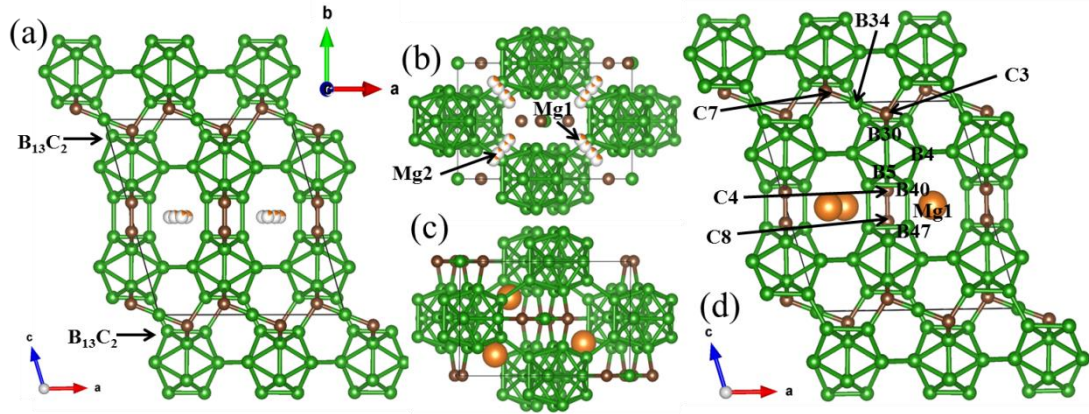


FIGURE 1. Atomic structure for $Mg_3B_{50}C_8$: (a) crystal structure, (b) Mg partial occupation sites, (c) the most stable atomic structure from DFT, and (d) the specific atomic location for the most stable atomic configuration. The B, C, and Mg atoms are represented by green, sienna, and orange balls, respectively. The partial occupation sites for Mg are represented by white-orange balls. All the atomic structures are visualized using VESTA software.⁴⁹

$Mg_3B_{50}C_8$ structure belongs to the $C2/m$ space group and the unit cell contains four B_{12} icosahedra, two C-B-C chains, and four C-C chains, as shown in Figure 1(a). The crystal structure of B_4C is composed of $B_{11}C$ icosahedron and C-B-C chain where the $B_{11}C$ icosahedron is connected to six C-B-C chains and six nearby icosahedra, forming a rhombohedral lattice unit with the $R\bar{3}m$ space group.⁹ Substituting the C atom in the $B_{11}C$ icosahedron with B atom leads to the boron rich boron carbide ($B_{13}C_2$).² Adding Mg into B_4C will significantly change the atomic structure of B_4C .³² The $Mg_3B_{50}C_8$ structure can be considered as two $B_{13}C_2$ supercells connecting through Mg atoms and direct icosahedral-icosahedral bonds (Figure 1(a)). Two C-C chains and three Mg atoms are located at the boundary of two $B_{13}C_2$ supercell, as shown in Figure 1(a). Four Mg sites in the unit cell were partially occupied (Figure.

1(b)) by three Mg atoms because of the electron balance which will be discussed below. To determine the ground state structure of $\text{Mg}_3\text{B}_{50}\text{C}_8$, we first constructed six possible atomic structures (Figure S1 of Supplemental Materials (SM)) according to various occupation sites, and then we performed the structure optimization using DFT. We selected the structure with the lowest energy (Figure 1(c)) for further simulations on chemical bonding and mechanical properties. The optimized lattice constant for $\text{Mg}_3\text{B}_{50}\text{C}_8$ are $a = 8.938 \text{ \AA}$, $b = 5.651 \text{ \AA}$, $c = 9.602 \text{ \AA}$, and $\beta = 105.86^\circ$, which agree very well with experimental values of $a = 8.939 \text{ \AA}$, $b = 5.670 \text{ \AA}$, $c = 9.610 \text{ \AA}$, and $\beta = 105.81^\circ$.³² It is worth noticing that the six different initial structures of $\text{Mg}_3\text{B}_{50}\text{C}_8$ are nearly converged to the same energy structure after geometry optimization, as shown in Table S1 of SM.

In order to validate our DFT simulations, we compared the details of our computed atomic structure with experiments. The specific atomic location for our model is shown in Figure 1(d). The bond lengths of B5-B30 and B4-B30 bonds within the B_{12} icosahedron are 1.744 \AA and 1.829 \AA , respectively. In contrast, the experimental measure values are 1.818 \AA and 1.843 \AA for these two bonds.³² The angles of B5-B30-B4, B30-B4-B5 and B4-B5-B30 are 60.16° , 57.58° , and 62.27° , respectively. The four icosahedra are connected via inter-icosahedral bonds (e.g. B47-B40 bond) with the bond distance of 1.833 \AA , compared to 1.866 \AA measured from experiment.³² The B_{12} layers are connected through the C-C chain (e.g. C4-C8) with the C-C bond length of 1.395 \AA (1.390 \AA in experiment) and C-B-C chain with the C-B chain bond (e.g. C7-B34) and C-B icosahedral-chain bond (C3-B30) of 1.448

Å (1.446 Å in experiment) and 1.619 Å (1.614 Å in experiment), respectively.³² The distance between the Mg1 atom and the B47 atom and between the Mg1 and B40 are 2.238 Å and 2.230 Å, respectively, compared to 2.335 Å and 2.326 Å from experiment.³² The C atoms are slightly far from Mg atoms with the distance of the Mg-C of 2.295 Å, compared to 2.167 Å from experiments.³²

The combination of B 2p orbitals and C 2p orbitals leads to the strong covalent bonds in both B₄C and Mg₃B₅₀C₈. The Mg atoms are not covalently bonded to the B and C atoms in the Mg₃B₅₀C₈ structure. Instead, the Mg atoms provide electrons to the B₁₂ icosahedral clusters. This can be derived from electron localization function (ELF) analysis⁴⁶ shown in the Figure 2.

The ELF analysis suggested that each B₁₂ icosahedron forms ten two-center-two-electron (2c-2e) bonds with nearby icosahedra and chains. While other two icosahedral-icosahedral (e.g. B40-B47) bonds cannot be considered as 2c-2e bond because the electron pair is not located in the center of the bond, as shown in Figure 2(a). In addition, the bond distance is 1.833 Å, larger than the normal B-B 2c-2e bond of 1.70 Å. Therefore, we consider this B-B bond as a three-center-two-electron (3c-2e) bond among 3 atoms B-B-Mg. Twelve B atoms in the icosahedron can provide 36 valence electrons in total and there are $10 + 2/3 \times 2 = 11\frac{1}{3}$ electrons involved in the extra-icosahedral bonding. This makes $24\frac{2}{3}$ electrons within the icosahedron. To satisfy Wade's rule that 26 electrons are required for stabilizing B₁₂ icosahedra,^{36,47} each icosahedron requires extra $1\frac{1}{3}$ electrons. Therefore, four B₁₂ icosahedra in the Mg₃B₅₀C₈ unit cell require $1\frac{1}{3} \times 4 = 5\frac{1}{3}$

electrons that can be transferred from Mg atoms and middle B atoms in C-B-C chains. Since two Mg atoms are located in the left part and only one Mg atom is located in the right part (Figure. 2(b)), the single Mg in the right forms two 3c-2e bonds giving $4/3$ electrons while each Mg in the left only forms one 3c-2e bond giving $2/3$ electrons. This indicates that Mg in the $Mg_3B_{50}C_8$ system involves in the 3c-2e bonds, leading to some covalent bonding character. According to the bonding analysis of Mg atoms, three Mg atoms can transfer $2 \times \frac{4}{3} + \frac{2}{3} = \frac{10}{3}$ electrons to four icosahedral clusters after subtracting the electrons required for 3c-2e bonds. Thus, four icosahedra still require $16/3 - 10/3 = 2$ electrons. The C-C bonds are all double bonds that cannot transfer extra electrons, while the middle boron in the C-B-C chain can transfer one electron to the icosahedron, just like $(B_{11}C)CBC$ structure.^{9,10} This makes the whole system satisfy the Wade's rule. Thus, the $Mg_3B_{50}C_8$ can be represented by $(Mg^{4/3+})_2(Mg^{2/3+})(B_{12}^{4/3-})_4(CB^+C)_2(C_2)_2$ based on the above bonding analysis. From our bonding analysis, three Mg atoms filled in four partial occupation sites makes the atomic structure exactly satisfy the Wade's rule. This may explain why the partial occupation sites exist in $Mg_3B_{50}C_8$ system. Compared to B_4C , more 3c-2e bonds form in $Mg_3B_{50}C_8$, suggesting that the metallic character is increased by adding Mg into B_4C .

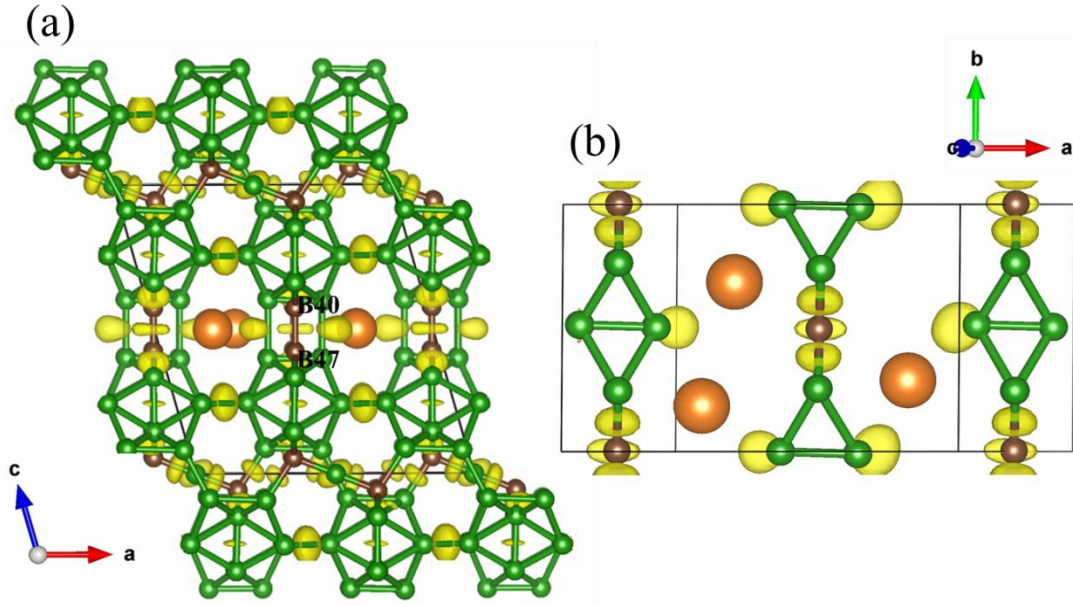


FIGURE 2. The isosurface (0.85) of electron localization function (ELF) analysis for $Mg_3B_{50}C_8$: (a) view along $[001]$ direction; (b) local view of Mg nearby region.

3.2 Elastic Properties of $Mg_3B_{50}C_8$

For elastic properties, we calculated the elastic moduli of $Mg_3B_{50}C_8$ leading to the bulk modulus $B_V = 217.38$ GPa and the shear modulus $G_V = 189.71$ GPa for Voigt values; and the bulk modulus $B_R = 213.89$ GPa and the shear modulus $G_R = 181.48$ GPa for Ruess values. The predicted elastic constant of $Mg_3B_{50}C_8$ is listed in the Table S2 of SM. Therefore, the bulk modulus $B = 215.63$ GPa and the shear modulus $G = 185.60$ GPa from the Voigt-Ruess-Hill approximation.

The ductility of metal alloys can be estimated using the Paugh criterion in which a ductile material has $B/G > 1.75$ where B and G are bulk modulus and shear modulus, respectively.⁴² Although this criterion is not well validated for superhard ceramics, we apply it to $Mg_3B_{50}C_8$ and compared to B_4C . The B/G for $Mg_3B_{50}C_8$ is 1.36, which is larger than that of B_4C (1.2).¹⁰ Although the B/G value for $Mg_3B_{50}C_8$ is still less than

ductile metals, it is 13.3% high than that of B₄C. This suggests that Mg₃B₅₀C₈ is more ductile than B₄C.

3.3 Ideal shear deformation of Mg₃B₅₀C₈

In order to understand the failure mechanisms of Mg₃B₅₀C₈, which is related to its ductility and fracture toughness, we performed pure shear deformation on Mg₃B₅₀C₈ along five plausible slip systems: (100)[001], (100)[010], (010)[001], (001)[$\bar{1}00$] and (001)[$\bar{1}\bar{1}0$]. Here we considered the low miller index planes (100), (010) and (001) as the plausible slip system. It is worth noticing that the (001)[$\bar{1}\bar{1}0$] slip system is analogous to the most plausible slip system (01 $\bar{1}\bar{1}$)[$\bar{1}101$] in B₄C.⁹ However, the strong C-C chain bond seems suppress the activation of this slip system compared to B₄C. The shear-stress-shear-strain relationships for these five slip systems are displayed in Figure 3(a), and compared to that of B₄C in Figure 3(b).⁹ The critical shear stress are 39.95 GPa, 28.87 GPa, 55.10 GPa, 37.25 GPa and 41.98 GPa for (100)[001], (100)[010], (010)[001], (001)[$\bar{1}00$], and (001)[$\bar{1}\bar{1}0$] slip systems, respectively. The critical shear stress refers to the shear stress barrier that activates the slip system. Therefore, the (100)[010] slip system has the minimum critical shear stress of 28.87 GPa among all 5 slip systems, indicating that it is the most plausible slip system for Mg₃B₅₀C₈. In contrast, the B₄C has the lowest critical shear strength of 38.97 GPa along the most plausible slip system (01 $\bar{1}\bar{1}$)[$\bar{1}101$] under finite shear deformation.⁹ Therefore, the intrinsic strength of Mg₃B₅₀C₈ is lower than that of B₄C. The shear-stress-shear-strain relationship for (100)[010] slip system displays the “plastic deformation” character in which a kink appears before failure. While the

shear stress just significantly drops after passing the elastic deformation region for other four slip systems.

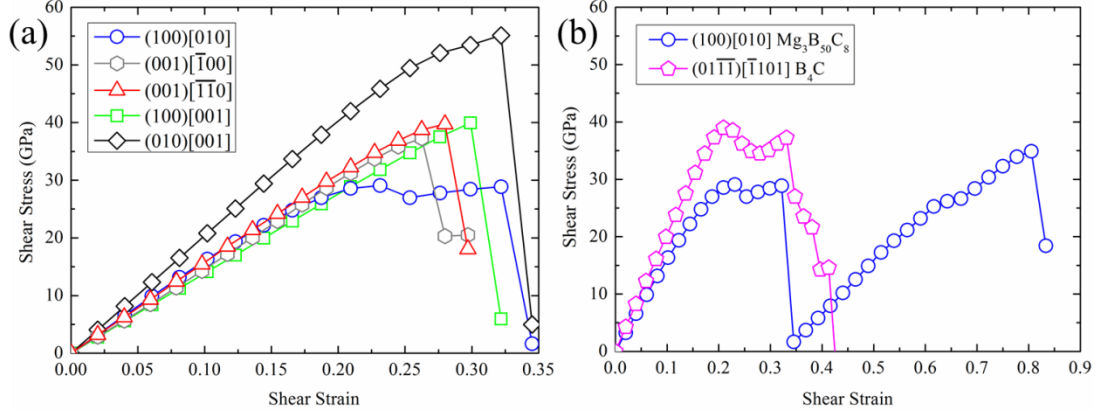


FIGURE 3. (a) The shear-stress-shear-strain relationship of $Mg_3B_{50}C_8$ for five plausible slip system under ideal shear deformation; (b) The shear-stress-shear-strain relationship of $Mg_3B_{50}C_8$ and B_4C under ideal shear deformation for the most plausible slip system $(100)[010]$ and $(01\bar{1})[\bar{1}101]$, respectively. The ideal shear strength of $Mg_3B_{50}C_8$ is much lower than that of B_4C .

We focus on the failure mechanism along the most plausible slip system $(100)[010]$ to understand the intrinsic failure mechanisms of $Mg_3B_{50}C_8$. To examine the detailed deformation process, we extended the shear-stress-shear-strain relationship for slip system $(100)[010]$ to 0.833 shear strain, as shown in Figure 3(b). The detailed failure process shown in Figure 4 is discussed below.

As the intact structure (Figure 4(a)) is deformed elastically to 0.231 shear strain corresponding to the maximum shear stress (Figure 4(b)), The inter-icosahedral B16-B23 bond is stretched from 1.776 to 2.473 Å because of the shear deformation. But this bond is not broken, as shown in the ELF analysis (Figure 5(a)). In addition, the Mg atoms are slight displaced. Particularly, the Mg3-B16 and Mg2-B24 distances

increase from 2.534 Å and 2.578 Å to 2.732 Å and 2.681 Å, respectively. As the shear strain continuously increases to 0.254, the B16-B23 bond is further stretched to 2.835 Å. However, ELF analysis in Figure 5(b) indicates that this bond is delocalized and softened, leading to the shear stress decreasing from 29.07 to 26.94 GPa. No B₁₂ icosahedra are deconstructed, as shown in Figure 4(c). As the shear strain further increases to 0.322, the B16-B23 bond is increased to 3.238 Å and broken. The B₁₂ icosahedra are still not constructed, as shown in Figure 4(d). This corresponds to the critical shear strain before the shear stress significantly drops. After the shear strain passes the critical shear strain and reaches to 0.345 (Figure 4(e)), both inter-icosahedral B16-B23 and B15-B24 bonds are broken. Meanwhile this process forms two new bonds of B15-B16 and B23-B24. In addition, the chain-icosahedral C3-B46 and C5-B42 bonds are both broken, while two new bonds of C3-C5 and B42-B46 are formed. This process leads to the icosahedral clusters slipped and the shear stress significantly decreasing from 28.87 to 1.65 GPa. However, no icosahedra are deconstructed in this process, suggesting the structure is not truly failed. Thus, we continuously shear it to the extended strain of 0.805 corresponding to the second critical shear stress of 34.90 GPa. The second critical stress of 34.90 is 20.1% higher than the first one of 29.07 GPa. No icosahedra are deconstructed as the system is sheared to 0.805 strain, as shown in Figure 4(f). After passing this critical shear strain, the icosahedra are just slipped again and are not deconstructed, as shown in Figure 4(g). The deformation behavior suggests that adding Mg to B₄C increases the metallic bonding character and the ductility of Mg₃B₅₀C₈ is drastically enhanced.

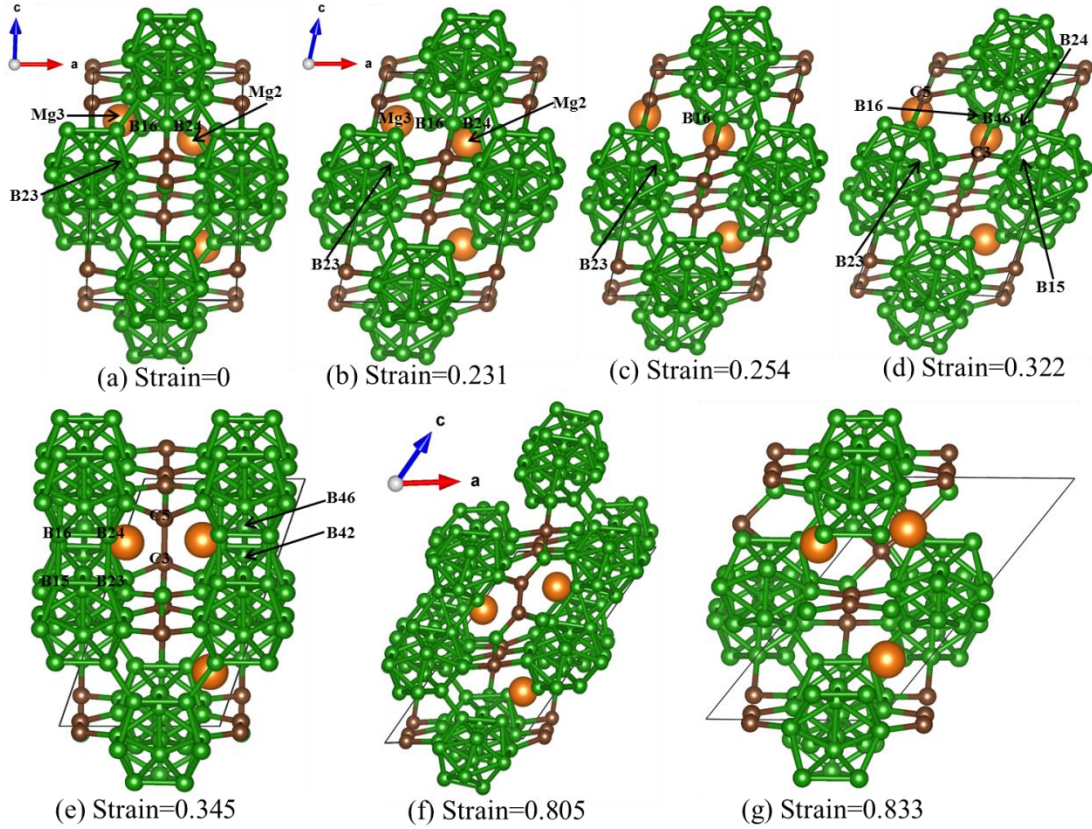


FIGURE 4. The structural evolution of $Mg_3B_{50}C_8$ system along $(100)[010]$ slip system under pure shear deformation: (a) Intact structure; (b) Structure at 0.231 shear strain corresponding to the maximum shear stress; (c) Structure at 0.254 shear strain with inter-icosahedral bond softening; (d) Structure at 0.322 shear strain before shear stress significantly release; (e) Structure at 0.345 shear strain after the icosahedra slip; (f) Structure at 0.805 shear strain corresponding to the 2nd maximum shear stress; (g) Structure at 0.833 shear strain with the second icosahedral slip. The B, C and Mg atoms are represented by green, sienna, and orange balls, respectively.

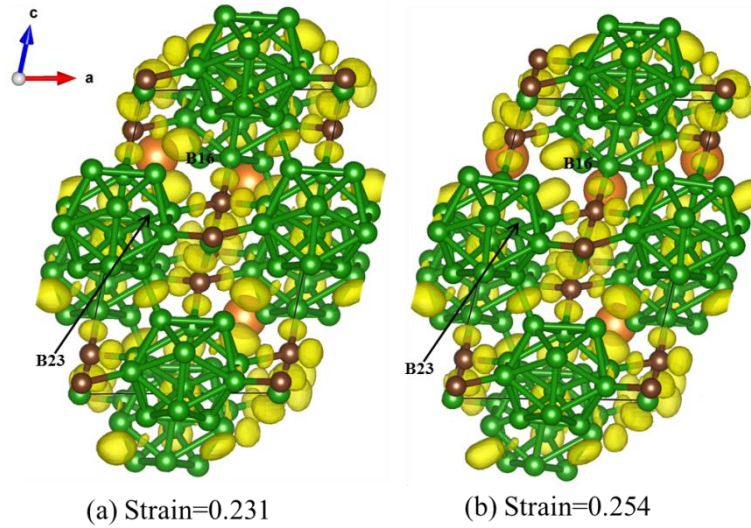


FIGURE 5. The isosurface (0.85) of the electron localization function (ELF) for shear along (100)[010] slip system: (a) The ELF at 0.231 shear strain showing the bonding of the B16-B23. (b) the ELF at 0.254 strain showing that the bond of B16-B23 is not localized as (a). The B, C and Mg atoms are represented by green, sienna, and orange balls, respectively.

The (001)[$\bar{1}00$] slip system has the secondary lowest critical shear stress of 37.25 GPa which is 29.4% higher than that of (100)[010] slip system. It is plausible to be activated under high stress conditions since it is the second plausible slip system. Therefore, we examined its failure mechanism, as shown in Figure 6. The intact structure is displayed in Figure 6(a). As the shear strain increases to 0.263, corresponding to the maximum shear stress, the B81-B89, B57-B89, B61-B93, and B69-B93 bonds are stretched from 1.818, 1.822, 1.826, and 1.807 Å to 2.295, 2.110, 2.084, and 2.202 Å, respectively, as shown in Figure 6(b). But the icosahedra are not deconstructed yet. As the shear strain further increases to 0.280, the B81-B89, B57-B89, B61-B93, and B69-B93 bonds are broken with the bond lengths increased to 3.539, 3.223, 3.135, and 3.491 Å, respectively, leading to the deconstruction of

icosahedra, as shown in Figure. 6(c). This process causes the shear stress decrease from 37.25 GPa to 20.30 GPa and the failure of the system.

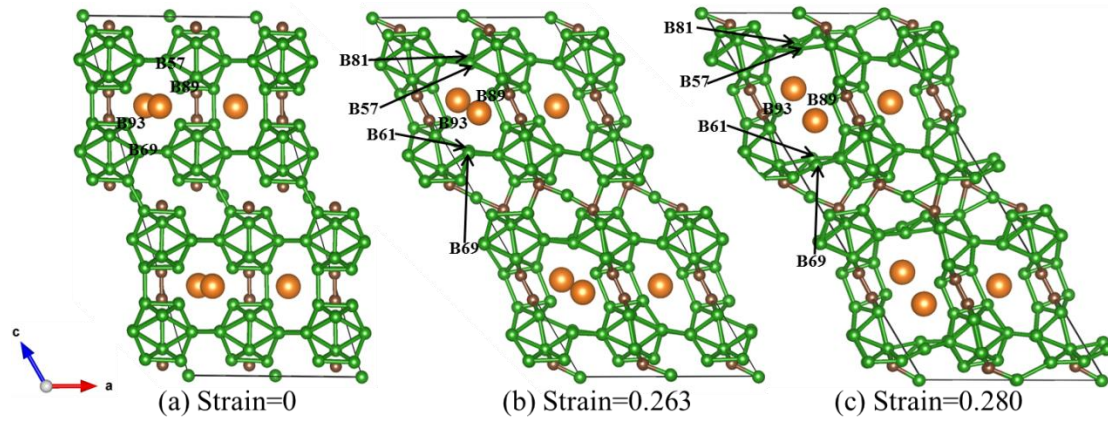


FIGURE 6. *Structural changes of $Mg_3B_{50}C_8$ system under pure shear deformation along $(001)[\bar{1}00]$ slip system: (a) Intact structure; (b) structure corresponding to the maximum shear stress; (c) failed structure showing the deconstruction of icosahedra. The B_{81} is behind B_{57} and is not shown in (a). The B, C and Mg atoms are represented by green, sienna and orange balls, respectively.*

3.4 Deformation mechanisms of $Mg_3B_{50}C_8$ under indentation stress condition

Indentation is an experimental approach to examine the deformation mechanisms of materials. However, the stress conditions are quite different compared to pure shear deformation. In order to understand the deformation mechanisms of $Mg_3B_{50}C_8$ under indentation stress conditions, we applied biaxial shear deformation along two slip systems: $(001)[\bar{1}00]$ and the $(100)[010]$ that have the lowest shear stress under the pure shear deformation. The shear-stress-shear-strain relationship shown in Figure 7 indicates that the critical shear stress of $(100)[010]$ slip system is 33.43 GPa while it is 29.22 GPa for $(001)[\bar{1}00]$ slip systems. Therefore, the $(001)[\bar{1}00]$ slip system is more favorable to be activated than $(100)[010]$ under indentation stress condition. In contrast, our pure shear deformation results suggested that $(100)[010]$ is more favorable under pure shear deformation. Therefore, the different applied stress

conditions could lead to different activated slip systems in $\text{Mg}_3\text{B}_{50}\text{C}_8$. Our pure shear deformation results suggest that the $\text{Mg}_3\text{B}_{50}\text{C}_8$ is 25.9% lower in strength compared to B_4C . However, under indentation conditions, the critical shear stress of $\text{Mg}_3\text{B}_{50}\text{C}_8$ is slight higher than that of B_4C (28.50 GPa),⁴⁸ as shown in Figure 7. This suggests that the intrinsic hardness of $\text{Mg}_3\text{B}_{50}\text{C}_8$ is slightly higher than that of B_4C , which is consistent with the measured microhardness of $\text{Mg}_3\text{B}_{50}\text{C}_8$.³²

It is worth to note that the microhardness may be related to the grain boundaries properties. To validate our simulation results, it may be worth to perform the nanoindentation experiments in the future study.

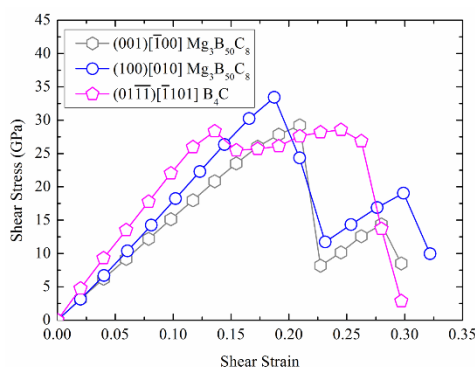


FIGURE 7. The shear-stress-shear-strain relationship of $\text{Mg}_3\text{B}_{50}\text{C}_8$ and B_4C for the most plausible slip system under biaxial shear deformation.

In order to understand the detailed failure mechanism, we examined the structural changes of $\text{Mg}_3\text{B}_{50}\text{C}_8$ under the biaxial shear deformation along the $(001)[\bar{1}00]$ slip system, shown in Figure 8. The intact structure is displayed in Figure 8(a). As the shear strain increases to 0.209, corresponding to the maximum shear stress, the B84-B66 and B84-B74 distances decrease from 2.872 Å and 2.887 Å to 2.609 Å and 2.640 Å, respectively, because of the compressive stress (Figure 8(b)). As the shear strain further increases to 0.227, the C-B-C chain interacts with nearby icosahedra, leading to the deconstruction of nearby B_{12} icosahedra, as shown in Figure.

8(c). Particularly, The C-B-C chain forms new bonds with B atoms in the icosahedra (e.g. B84-B66, B84-B74, and C3-B66).

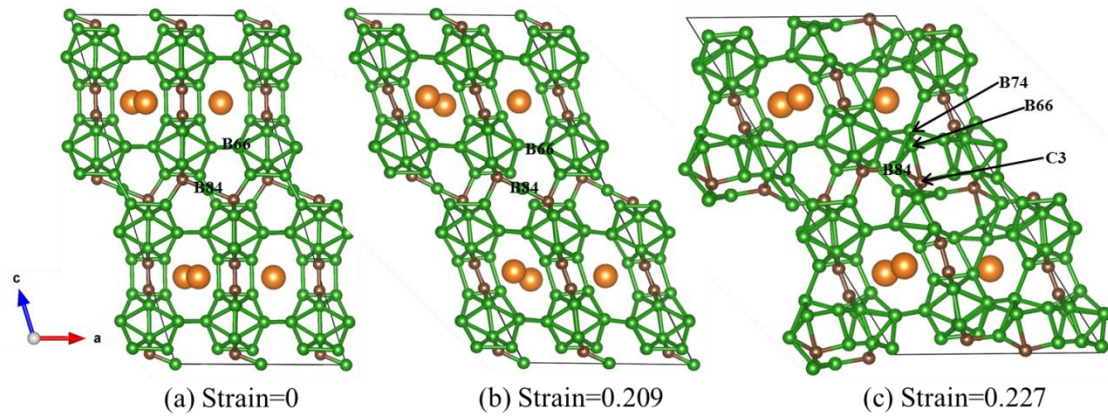


FIGURE 8. The structural changes of $Mg_3B_{50}C_8$ under the biaxial shear deformation along the $(001)[\bar{1}00]$ slip system: (a) Intact structure; (b) structure before failure; (c) failed structure showing the deconstruction of icosahedra. The B_{74} is behind B_{66} and not shown in the (a) and (b). The B, C and Mg atoms are represented by green, sienna and orange balls, respectively.

Since the $(100)[010]$ slip system is the most plausible activated system under pure shear deformation, we examined its failure mechanisms under indentation stress conditions even it has a higher critical shear stress than that of $(001)[\bar{1}00]$ slip system. The detailed failure process is shown in Figure 9. The intact structure is displayed in Figure 9(a). As the shear strain increases to 0.187, corresponding to the maximum shear stress, the B14-B50 bond is stretched from 1.784 Å from 1.843 Å (Figure 9(b)). As the shear strain increases to 0.209, the B14-B50 bond is further stretched with the bond length increasing to 2.033 Å, as shown in Figure 9(c). As the shear strain further increases to 0.231, both B25-B36 and B39-B29 bonds within the B_{12} icosahedron are broken with both bond lengths stretched from 1.841 Å to 2.787 Å, as shown in Figure

9(d). This leads to the deconstruction of icosahedra and failure of the system.

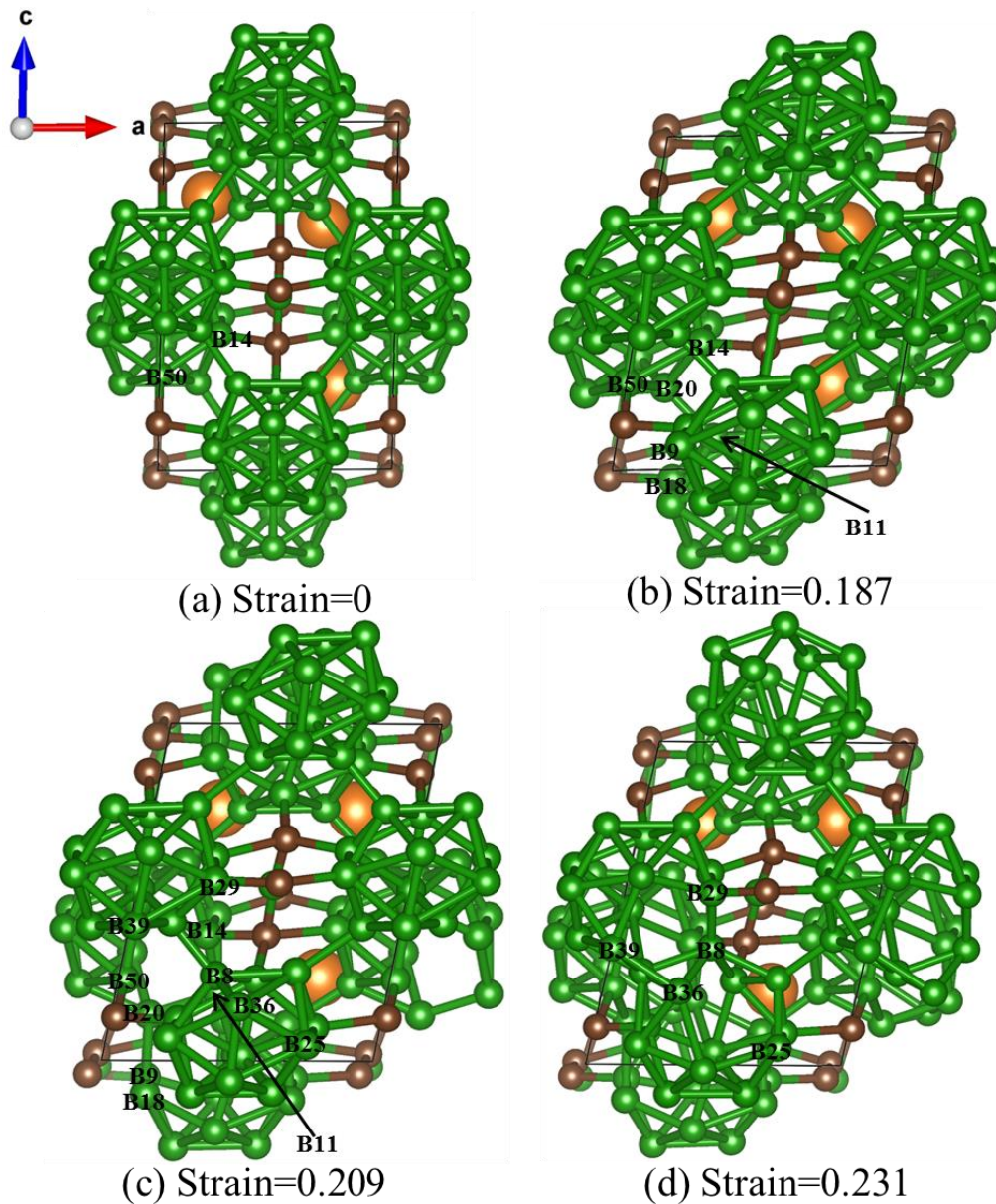


FIGURE 9. The structural changes of $Mg_3B_{50}C_8$ under the biaxial shear deformation along the $(100)[010]$ slip system: (a) Intact structure; (b) Structure at 0.187 shear strain corresponding to the maximum shear stress; (c) Structure at 0.209 shear strain; (d) failed structure at 0.231 shear strain. The B, C and Mg atoms are represented by green, sienna and orange balls, respectively.

4. Conclusion

In summary, we have examined the structure, the chemical bonding and mechanical properties of recent synthesized $\text{Mg}_3\text{B}_{50}\text{C}_8$ using DFT simulations. Our results suggest that doping metal elements into B_4C is an excellent approach to enhance the mechanical properties. The major findings are listed below.

- The new synthesized $\text{Mg}_3\text{B}_{50}\text{C}_8$ still satisfies the electron counting (Wade's) rules and it can be represented as $(\text{Mg}^{4/3+})_2(\text{Mg}^{2/3+})(\text{B}_{12}^{4/3-})_4(\text{CB}^+\text{C})_2(\text{C}_2)_2$ based on the ELF analysis.
- We found that the (100)[010] slip system is the most plausible slip system for $\text{Mg}_3\text{B}_{50}\text{C}_8$ under pure shear deformation. However, the B_{12} icosahedra are just slipped without deconstruction until extended shear strain of 0.833, suggesting that the ductility is significantly enhanced compared to B_4C .
- Under indentation stress conditions, the most plausible slip system is changed to (001)[$\bar{1}00$] for $\text{Mg}_3\text{B}_{50}\text{C}_8$, suggesting that the applied stress conditions can significantly affect the activated slip systems. The icosahedral clusters could be deconstructed under indentation stress conditions because of the interaction of C-B-C chain and icosahedra under highly compressive conditions.

Acknowledgement:

This work is supported by National Science Foundation (CMMI-1727428).

Supplemental Material (SM) The SM include the possible atomic structures of $\text{Mg}_3\text{B}_{50}\text{C}_8$, the computed elastic constant matrix C_{ij} .

References:

1. Yan XQ, Tang Z, Zhang L, Guo JJ, Jin CQ, Zhang Y, et al. Depressurization amorphization of single-crystal boron carbide. *Phys Rev Lett*. 2009;102(7):075505.
2. Thevenot F. Boron carbide—a comprehensive review. *J Eur Ceram Soc*. 1990;6(4):205-225.
3. Suri AK, Subramanian C, Sonber JK, Murthy T. Synthesis and consolidation of boron carbide: a review. *Int Mater Rev*. 2010;55(1):4-40.
4. Shirai K. Electronic structures and mechanical properties of boron and boron-rich crystals (part 2). *J Superhard Mater*. 2010;32(5):336-345.
5. Sezer AO, Brand JI. Chemical vapor deposition of boron carbide. *Mat Sci Eng B-Solid*. 2001;79(3):191-202.
6. Fanchini G, McCauley JW, Chhowalla M. Behavior of disordered boron carbide under stress. *Phys Rev Lett*. 2006;97(3):035502.
7. Emin D. Unusual properties of icosahedral boron-rich solids. *J Solid State Chem*. 2006;179(9):2791-2798.
8. Domnich V, Reynaud S, Haber RA, Chhowalla M. Boron carbide: structure, properties, and stability under stress. *J Am Ceram Soc*. 2011;94(11):3605-3628.
9. An Q, Goddard III WA, Cheng T. Atomistic explanation of shear-induced amorphous band formation in boron carbide. *Phys Rev Lett*. 2014;113(9):095501.
10. An Q, Goddard III WA. Microalloying boron carbide with silicon to achieve dramatically improved ductility. *J Phys Chem Lett*. 2014;5(23):4169-4174.
11. Chen MW, McCauley JW, LaSalva JC, Hemker KJ. Microstructural characterization of commercial hot-pressed boron carbide ceramics. *J Am Ceram Soc*. 2005;88(7):1935-1942.
12. Chen M, McCauley JW, Hemker KJ. Shock-induced localized amorphization in boron carbide. *Science*. 2003;299(5612):1563-1566.
13. Tang B, An Q, Goddard III WA. Improved ductility of boron carbide by

- microalloying with boron suboxide. *J Phys Chem C*. 2015;119(43):24649-24656.
14. Khan AU, Etzold AM, Yang XK, Domnich V, Xie KY, Hwang C, et al. Locating Si atoms in Si-doped boron carbide: a route to understand amorphization mitigation mechanism. *Acta Mater*. 2018;157:106-113.
 15. Guo DZ, Song SX, Luo RC, Goddard III WA, Chen MW, Reddy KM, et al. Grain boundary sliding and amorphization are responsible for the reverse Hall-Petch relation in superhard nanocrystalline boron carbide. *Phys Rev Lett*. 2018;121(14):145504.
 16. An Q, Goddard III W A. Improved ductility of B₁₂ icosahedra-based superhard materials through icosahedral slip. *J Phys Chem C*. 2017;121(21):11831-11838.
 17. Frage N, Levin L, Frumin N, Gelbstein M, Dariel MP. Manufacturing B₄C-(Al,Si) composite materials by metal alloy infiltration. *J Mater Process Technol*. 2003;143:486-490.
 18. Tavsanoğlu T, Jeandin M, Addemir O, Yucel O. A functionally graded multilayer approach to the synthesis of boron containing ceramic thin films. *Solid State Sci*. 2012;14(11-12):1717-1721.
 19. Li HB, Zheng YT, Han JC, Zhou LJ. Effect of reactant Ti/B₄C ratio on the stoichiometry and mechanical properties of h-BN-Ti(C,N) prepared by combustion synthesis. *Mater Sci Eng A*. 2011;528(6):2380-2384.
 20. Zeng XJ, Liu WL. Enhanced sintering of boron carbide-silicon composites by silicon. *J Mater Eng Perform*. 2016;25(11):5014-5019.
 21. Wang JH, Guo XL, Qin JN, Zhang D, Lu WJ. Morphology evolution of alpha phase in investment cast titanium matrix composites with B₄C additions. *J Mater Sci*. 2015;50(17):5674-5683.
 22. Jia L, Li SF, Imai H, Chen B, Kondoh K. Size effect of B₄C powders on metallurgical reaction and resulting tensile properties of Ti matrix composites by in-situ reaction from Ti-B₄C system under a relatively low temperature. *Mater Sci Eng A*. 2014;614:129-135.
 23. Chen HS, Zhan YY, Nie HH, Wang JF, Wang WX, Zhou J, et al. The

microstructure and mechanical properties of the B₄C/Cu matrix composite fabricated by SPS-HR. *Mater Sci Technol.* 2018;34(12):1460-1467.

24. Aizenshtein M, Froumin N, Frage N, Dariel MP. Interface phenomena in the B₄C/(Me-Ti) systems (Me = Cu, Au and Sn). *J Mater Sci.* 2005;40(9-10):2325-2327.

25. Aizenshtein M, Froumin N, Frage N, Dariel MP. Interface interaction and wetting behaviour in B₄C/(Me-Ti) systems (Me = Cu, Ag, Sn and Au). *Mater Sci Eng A.* 2005;395(1-2):180-185.

26. Tsai JL, Tsai WC, Lin YC, Wu SC. Microstructure and magnetic properties of FePt(B₄C) and FePt(B₄C-Ag) granular films with perpendicular magnetization. *J Alloys Compd.* 2013;579:12-17.

27. Jia L, Wang XS, Chen BA, Imai H, Li SF, Lu ZL, et al. Microstructural evolution and competitive reaction behavior of Ti-B₄C system under solid-state sintering. *J Alloys Compd.* 2016;687:1004-1011.

28. Tang JX, Cheng JH, Zeng ZQ, Miao HZ. Diffusion path and reaction mechanism between Ti and B₄C. *J Inorg Mater.* 2000;15(5):884-888.

29. Mashhadi M, Taheri-Nassaj E, Sglavo V M, Sarpoolaky H, Ehsani N. Effect of Al addition on pressureless sintering of B₄C. *Ceram Int.* 2009;35(2):831-837.

30. Ghasali E, Alizadeh M, Ebadzadeh T, Pakseresht AH, Rahbari A. Investigation on microstructural and mechanical properties of B₄C-aluminum matrix composites prepared by microwave sintering. *J Mater Res Technol.* 2015;4(4):411-415.

31. Ghasali E, Alizadeh M, Ebadzadeh T. Mechanical and microstructure comparison between microwave and spark plasma sintering of Al-B₄C composite. *J Alloys Compd.* 2016;655:93-98.

32. Adasch V, Schroeder M, Kozzot D, Ludwig T, Vojteer N, Hillebrecht H. Synthesis, crystal Structure, and properties of Mg_xB₅₀C₈ or Mg_x(B₁₂)₄(CBC)₂(C₂)₂ (x=2.4-4). *J Am Chem Soc.* 2010;132(39):13723-13732.

33. Teter DM. Computational alchemy: the search for new superhard materials. *MRS Bull.* 1998;23(1):22-27.

34. Hillebrecht H, Vojteer N, Sagawe V, Hofmann K, Albert B. Synthesis and

characterization of Li - containing boron carbide r - $\text{Li}_{-1}\text{B}_{13}\text{C}_2$. *Z Anorg Allg Chem.* 2018;doi.org/10.1002/zaac.201800289

35. Perdew JP, Burke K, Ernzerhof M. Generalized gradient approximation made simple. *Phys Rev Lett.* 1997;78(7):1396-1396.
36. Wade K. The structural significance of the number of skeletal bonding electron-pairs in carboranes, the higher boranes and borane anions, and various transition-metal carbonyl cluster compounds. *J Chem Soc D.* 1971;(15):792-793.
37. Kresse G, Hafner J. Ab initio Hellmann-Feynman molecular-dynamics for liquid-metals. *J Non-Cryst Solids.* 1993;156:956-960.
38. Kresse G, Furthmuller J. Efficiency of ab-initio total energy calculations for metals and semiconductors using a plane-wave basis set. *Comp Mater Sci.* 1996;6(1):15-50.
39. Kresse G, Furthmuller J. Efficient iterative schemes for ab initio total-energy calculations using a plane-wave basis set. *Phys Rev B.* 1996;54(16):11169-11186.
40. Kresse G, Joubert D. From ultrasoft pseudopotentials to the projector augmented-wave method. *Phys Rev B* 1999;59(3):1758-1775.
41. Blochl PE, Jepsen O, Andersen OK. Improved tetrahedron method for brillouin-zone integrations. *Phys Rev B.* 1994;49(23):16223-16233.
42. Pugh SF. Relations between the elastic moduli and the plastic properties of polycrystalline pure metals. *Phil Mag.* 1954;45(367):823-843.
43. Le Page Y, Saxe P. Symmetry-general least-squares extraction of elastic data for strained materials from ab initio calculations of stress. *Phys Rev B.* 2002;65(10):104104.
44. Hill R. The elastic behaviour of a crystalline aggregate. *Proc Phys Soc. A.* 1952;65(5):349.
45. Li B, Sun H, Chen CF. Large indentation strain stiffening in nanotwinned cubic boron nitride. *Nat Commun.* 2014;5:4965.
46. Silvi B, Savin A. Classification of chemical-bonds based on topological analysis of electron localization functions. *Nature.* 1994;371(6499):683-686.

47. Mingos D. A general theory for cluster and ring compounds of the main group and transition elements. *Nature Phys Sci.* 1972;236(68):99-102.
48. An Q, Goddard III WA, Xie KY, Sim GD, Hemker KJ, Munhollon T, et al. Superstrength through nanotwinning. *Nano Lett.* 2016;16(12):7573-7579.
- 49 Momma K, Izumi F. VESTA 3 for three-dimensional visualization of crystal, volumetric and morphology data. *J Appl Crystallogr.* 2011;44:1272-1276.

Figure Captions:

FIGURE 1. Atomic structure for $Mg_3B_{50}C_8$: (a) crystal structure, (b) Mg partial occupation sites, (c) the most stable atomic structure from DFT, and (d) the specific atomic location for the most stable atomic configuration. The B, C, and Mg atoms are represented by green, sienna, and orange balls, respectively. The partial occupation sites for Mg are represented by white-orange balls. All the atomic structures are visualized using VESTA software.⁴⁹

FIGURE 2. The isosurface (0.85) of electron localization function (ELF) analysis for $Mg_3B_{50}C_8$: (a) view along [001] direction; (b) local view of Mg nearby region.

FIGURE 3. (a) The shear-stress-shear-strain relationship of $Mg_3B_{50}C_8$ for five plausible slip system under ideal shear deformation; (b) The shear-stress-shear-strain relationship of $Mg_3B_{50}C_8$ and B_4C under ideal shear deformation for the most plausible slip system (100)[010] and (01 $\bar{1}$)[$\bar{1}$ 101], respectively. The ideal shear strength of $Mg_3B_{50}C_8$ is much lower than that of B_4C .

FIGURE 4. The structural evolution of $Mg_3B_{50}C_8$ system along (100)[010] slip system under pure shear deformation: (a) Intact structure; (b) Structure at 0.231 shear strain corresponding to the maximum shear stress; (c) Structure at 0.254 shear strain with inter-icosahedral bond softening; (d) Structure at 0.322 shear strain before shear stress significantly release; (e) Structure at 0.345 shear strain after the icosahedra slip; (f) Structure at 0.805 shear strain corresponding to the 2nd maximum shear stress; (g) Structure at 0.833 shear strain with the second icosahedral slip. The B, C and Mg atoms are represented by green, sienna, and orange balls, respectively.

FIGURE 5. The isosurface (0.85) of the electron localization function (ELF) for shear along (100)[010] slip system: (a) The ELF at 0.231 shear strain showing the bonding of the B16-B23. (b) the ELF at 0.254 strain showing that the bond of B16-B23 is not localized as (a). The B, C and Mg atoms are represented by green, sienna, and orange balls, respectively.

FIGURE 6. Structural changes of $\text{Mg}_3\text{B}_{50}\text{C}_8$ system under pure shear deformation along $(001)[\bar{1}00]$ slip system: (a) Intact structure; (b) structure corresponding to the maximum shear stress; (c) failed structure showing the deconstruction of icosahedra. The B_{81} is behind B_{57} and is not shown in (a). The B, C and Mg atoms are represented by green, sienna and orange balls, respectively.

FIGURE 7. The shear-stress-shear-strain relationship of $\text{Mg}_3\text{B}_{50}\text{C}_8$ and B_4C for the most plausible slip system under biaxial shear deformation.

FIGURE 8. The structural changes of $\text{Mg}_3\text{B}_{50}\text{C}_8$ under the biaxial shear deformation along the $(001)[\bar{1}00]$ slip system: (a) Intact structure; (b) structure before failure; (c) failed structure showing the deconstruction of icosahedra. The B_{74} is behind B_{66} and not shown in the (a) and (b). The B, C and Mg atoms are represented by green, sienna and orange balls, respectively.

FIGURE 9. The structural changes of $\text{Mg}_3\text{B}_{50}\text{C}_8$ under the biaxial shear deformation along the $(100)[010]$ slip system: (a) Intact structure; (b) Structure at 0.187 shear strain corresponding to the maximum shear stress; (c) Structure at 0.209 shear strain; (d) failed structure at 0.231 shear strain. The B, C and Mg atoms are represented by green, sienna and orange balls, respectively.